

Short Communication

## Bimetallic Nitride NiWN<sub>2</sub>/ Nitrogen-doped Reduced Graphene Oxide Nanocomposites as High-Performance Counter Electrode Materials for Dye-Sensitized Solar Cells

Jihong Jiang<sup>1</sup>, Zuquan Jin<sup>1,\*</sup>, Jianhua Yao<sup>2</sup>, Xiuli Yang<sup>3</sup>, Chuansheng Xiong<sup>1</sup>, Yong Yu<sup>1</sup>, Ning Li<sup>1</sup> and Xiaoying Zhang<sup>1,\*</sup>

<sup>1</sup> Engineering Research Center of Concrete technology in marine environment, Ministry of Education, Qingdao University of Technology, Qingdao, 266033, P. R. China

<sup>2</sup> Qingdao Institute of Bioenergy and Bioprocess Technology, Chinese Academy of Sciences, Qingdao, 266101, P. R. China

<sup>3</sup> Qingdao Pony Test Co., Ltd., Jinshui Road 36, Qingdao, 266101, P. R. China

\*E-mail: [jinquan@126.com](mailto:jinquan@126.com); [zhangxy@qibebt.ac.cn](mailto:zhangxy@qibebt.ac.cn)

Received: 15 September 2020 / Accepted: 3 November 2020 / Published: 30 November 2020

Inspired by bimetallic sulfides and oxides, bimetallic nitride NiWN<sub>2</sub>/ Nitrogen-doped reduced graphene oxide (NiWN<sub>2</sub>/N-RGO) nanocomposites were prepared successfully through the hydrothermal method, and employed as high performance platinum-free counter electrodes (CEs) for dye-sensitized solar cells (DSCs). In the NiWN<sub>2</sub>/N-RGO CEs, NiWN<sub>2</sub> nanoparticles were anchored on the surface of N-RGO. Benefiting from the synergistic effects of the high electrocatalytic activity from NiWN<sub>2</sub> and the efficient electronic/ionic mixed conducting network provided by N-RGO, DSCs with NiWN<sub>2</sub>/N-RGO achieved an efficiency of 7.04%, which was up to 95% of that of a Pt CE (7.48%). Such an effective and versatile strategy may be extended to other bimetallic nitrides for use as inexpensive platinum-free CEs.

**Keywords:** bimetallic nitrides; NiWN<sub>2</sub>/N-RGO; counter electrode; dye-sensitized solar cells; platinum-free

### 1. INTRODUCTION

Dye-sensitized solar cells (DSCs) have been increasingly studied due to their environmental friendliness, simple preparation, low cost and high theoretical photoelectric conversion efficiency [1]. A DSC is composed of a dye-sensitized nanocrystalline TiO<sub>2</sub> photoanode, electrolyte and counter electrode (CE). As an important part of DSCs, the main functions of the CE is to catalyse the reduction of the redox couple in the electrolyte along with receiving and transmitting the electrons from the external circuit. At present, the CE is usually made of Pt because of its high catalytic activity and good

conductivity. However, the scarce resources and high price of Pt limit the industrial application of DSCs. In addition, Pt electrodes will corrode in electrolytes containing  $I/I_3^-$  redox couples [2]. In the past twenty years, researchers have been committed to developing inexpensive CE materials with excellent performance to replace Pt. Various materials have been developed, such as carbon materials, metal materials, conductive polymer materials, transition metal compound materials and composite materials [3-7].

Transition metal nitrides have become one of the most promising candidates due to their modifiable composition and molecular structure. In 2009, Professor Gao reported TiN nanotube arrays as DSC CEs for the first time [8]. They prepared  $TiO_2$  nanotube arrays by anodizing Ti foils and then nitrated the  $TiO_2$  nanotube arrays into TiN nanoarrays in an ammonia atmosphere at  $800^\circ C$ ; these arrays were then used as CE materials in DSC. The photovoltaic performance of DSCs with TiN nanoarrays is better than that of a Pt CE. Subsequently, a series of nitride materials as CEs were explored and proven to have good catalytic activity, such as MoN, WN,  $Fe_2N$ , CrN, VN, and  $Ni_3N$ , along with some related composite materials [9-12]. Nevertheless, their catalytic activity needs to be further enhanced to replace Pt.

Recently, some bimetallic sulfides and oxides have been developed, which have higher catalytic activity than their single metal compounds. For example, transparent  $NiCo_2S_4$  nanoparticles as a CE have been prepared by electrophoresis on FTO; this material has electrocatalytic activity that is equivalent to that of a Pt CE [13]. A  $NiCo_2O_4$ /carbon black ( $NiCo_2O_4/C$ ) composite material has been prepared by the solution method and served as the CE of dye-sensitized solar cells. DSCs with  $NiCo_2O_4/C$  achieve a power conversion efficiency of 6.27%, which is much higher than that of  $NiO/C$  (5.07%) and  $Co_3O_4/C$  (4.82%) [14]. It has been found that bimetallic compounds possess enhanced electrocatalytic performance, which is attributed to the synergistic effect between their metallic ions [15-17].

Inspired by previous work, bimetallic nitride  $NiWN_2$  is expected to be an interesting candidate for further enhancing the electrochemical performance of DSCs. Considering that nanoparticles easily agglomerate, electronic nanowiring by nitrogen-doped reduced graphene oxide (N-RGO) may be a good alternative, which provides multiple pathways for electron transfer, an extremely high surface/volume ratio for better electrode–electrolyte contact, and the fast diffusion of electrolyte species. Herein,  $NiWN_2/NG$  nanocomposites were prepared in which  $NiWN_2$  nanoparticles were tightly attached to N-RGO films. This distinctive structure makes the composites exhibit a synergistic effect between  $NiWN_2$  and N-RGO. The  $NiWN_2/N-RGO$  composite CE exhibits excellent electrocatalytic properties for the reduction of  $I_3^-$ . Moreover, the composite presents a decent energy conversion efficiency of 7.08%, which is up to 95% of that of a Pt CE (7.48%). To the best of our knowledge, this is the first time that  $NiWN_2/N-RGO$  has been utilized as a CE for DSC applications. The strategy presented here may be extended to selectively fabricate other bimetallic nitride CEs for DSC applications.

## 2. EXPERIMENTAL

### 2.1 Preparation of NiWN<sub>2</sub>/N-RGO

NiWO<sub>4</sub> was prepared by a hydrothermal synthesis and treated at 800 °C for 3 h in an ammonia atmosphere to obtain ternary nitrides. The specific method was to use sodium tungstate as the tungsten source, nickel nitrate as the metal source, polyethylene glycol 400 and graphene oxide (GO) as the surfactant. A mixture of these materials was stirred evenly, and then transferred into a hydrothermal reactor and treated at 200 °C for 12 h. After the temperature dropped to room temperature, the precipitate was sequentially washed and filtered 3 times with distilled water and absolute ethanol, and then the sample was placed in an 80 °C oven to obtain the metal oxide NiWO<sub>4</sub>/GO. NiWN<sub>2</sub>/N-RGO was obtained by calcining NiWO<sub>4</sub>/GO in an NH<sub>3</sub> atmosphere for 3 h. The specific heating process was as follows: room temperature to 300 °C at 5 °C min<sup>-1</sup>; 300 to 700 °C at 2 °C min<sup>-1</sup>; 700 to 800 °C at 1 °C min<sup>-1</sup>, held at 800 °C for 3 h, and then cooled to room temperature at a rate of 5 °C min<sup>-1</sup>. Without adding GO to the hydrothermal reactor, NiWN<sub>2</sub> could be obtained using the same preparation method.

### 2.2 Assembly of DSCs

A TiO<sub>2</sub> photoanode of DSC was constructed as described in the literature. The electrolyte was composed of 0.06 M lithium iodide, 0.03 M iodine, 0.1 M guanidine isothiocyanate and 0.5 M tert-butylpyridine in acetonitrile. The active area of the DSC without special instructions in this article was 0.16 cm<sup>2</sup> (0.4 cm×0.4 cm).

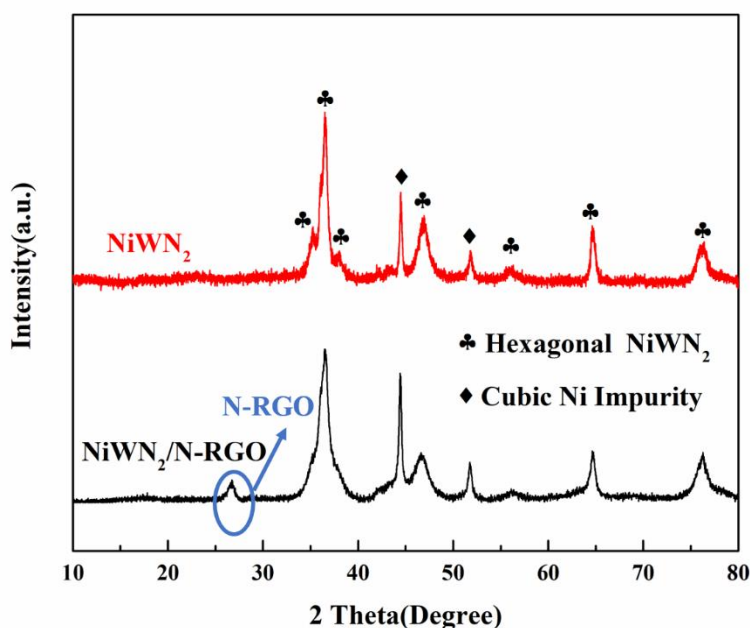
### 2.3 Sample Characterizations

The morphology and structure of the NiWN<sub>2</sub>/N-RGO composite material were determined by scanning electron microscopy (SEM, S-4800, Hitachi, Japan, the electron beam spot size was 3 nm and a high voltage of 15 kV was used) and transmission electron microscopy (TEM, TECNAI F20 S-TWIN, FEI, USA, acceleration voltage of 120 kV) observations. X-ray diffraction (XRD) was conducted with an anode material of copper and a (K $\alpha$ ) radiation source, a wavelength of 0.154 056 nm, a working voltage of 40 kV, a working current of 40 mA; additionally, the scanning range was 10~80°. The chemical state of NiWN<sub>2</sub>/N-RGO was measured by X-ray photoelectron spectroscopy (XPS, ESCALAB250, Thermo VG, U.S.). Cyclic voltammetry (CV), Potentiodynamic polarization and electrochemical impedance spectroscopy (EIS) were performed with a Zahnerennium electrochemical workstation using symmetrical thin-layer cells. CV was carried out in a three-electrode system at -0.6 V to 0.8 V with 20 mV/s, where the obtained NiWN<sub>2</sub>/N-RGO served as work electrode, Pt foil used as a CE and the Ag/Ag<sup>+</sup> as a reference electrode. EIS measurements were performed with an AC voltage of 10 mV amplitude in the frequency range between 100 kHz and 100 mHz at room temperature. The Potentiodynamic polarization measurements were obtained in a symmetrical cell fabricated with two identical NiWN<sub>2</sub>/N-RGO, NiWN<sub>2</sub> and Pt CEs from 0 to 0.6 V with 20 mV/s.

### 3. RESULTS AND DISCUSSION

#### 3.1. Structural and morphological analysis of NiWN<sub>2</sub>/N-RGO

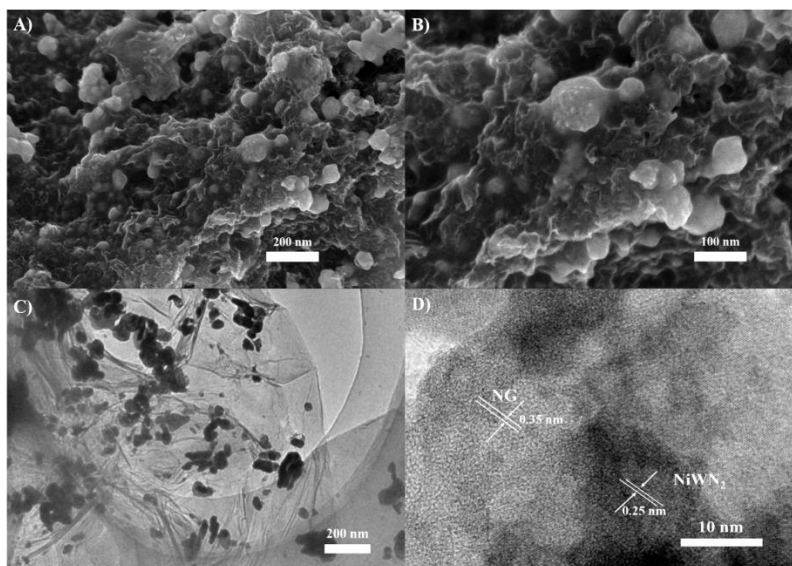
The crystal structure of the NiWN<sub>2</sub> and NiWN<sub>2</sub>/N-RGO films is shown in Figure 1. The diffraction peaks at 35.2, 36.4, 37.9, 46.8, 55.8, 64.6 and 76.3° are attributed to the (006), (101), (012), (104), (015), (107), (110) and (113) planes of hexagonal-phase NiWN<sub>2</sub>, respectively. In the XRD patterns of NiWN<sub>2</sub> and NiWN<sub>2</sub>/N-RGO, the characteristic peaks at approximately 44.3 and 51.8° are well matched to cubic-phase Ni (PDF No. 89-7128). This result indicates that the nitriding process from NiWO<sub>4</sub> to NiWN<sub>2</sub> under NH<sub>3</sub> conditions is accompanied by the formation of Ni, which is consistent with the results of previous studies [18]. Compared with NiWN<sub>2</sub>, a relatively dull diffraction peak at approximately 25° is observed in the NiWN<sub>2</sub>/N-RGO film, which is assigned to the (002) plane of N-RGO. These results prove the successful synthesis of NiWN<sub>2</sub>/N-RGO.



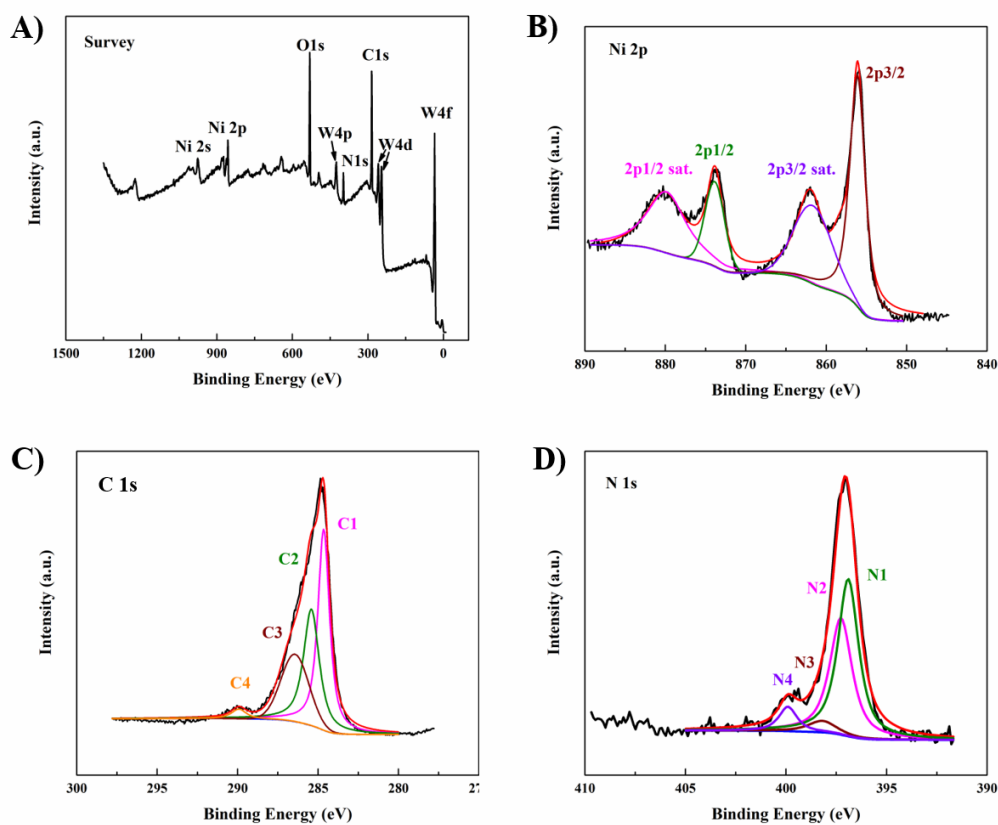
**Figure 1.** XRD patterns of the NiWN<sub>2</sub> and NiWN<sub>2</sub>/N-RGO films.

Figure 2 shows the SEM and TEM images of the NiWN<sub>2</sub>/N-RGO composite nanomaterial. From Figure 2A and 2B, it can be seen that the size of the NiWN<sub>2</sub> nanoparticles is 60~80 nm, and their surface is covered with a wrinkled N-RGO nanosheet layer, which enhances the thermodynamically stable bending of the nanocomposite material. In addition, the introduction of N-RGO can effectively avoid the agglomeration of NiWN<sub>2</sub> nanoparticles and ensure that the NiWN<sub>2</sub>/N-RGO nanocomposites have a large specific surface area, resulting in abundant catalytically active sites. To further study the morphological characteristics of NiWN<sub>2</sub>/N-RGO, NiWN<sub>2</sub>/N-RGO was characterized by TEM. From Figure 2C, small dark spots of uniform size can be observed, indicating that the NiWN<sub>2</sub> nanoparticles are highly dispersed in N-RGO. From the HRTEM image (Figure 2D), the lattice fringes of these small dark spots can be clearly observed. The lattice spacing value is 0.25 nm, which matches the (101) plane

of hexagonal NiWN<sub>2</sub>, further revealing the high crystallinity of NiWN<sub>2</sub>. The bright contrast area shows a layer spacing of 0.35 nm, which corresponds to the N-RGO nanosheet [19], which is consistent with the XRD test results.



**Figure 2.** Typical SEM (A and B), TEM (C) and HRTEM (D) images of NiWN<sub>2</sub>/N-RGO.



**Figure 3.** (A) Full-range XPS spectra, (B) Ni 2p XPS spectrum, (C) C 1s XPS spectrum and (D) N 1s XPS spectrum of NiWN<sub>2</sub>/N-RGO.

The surface elemental composition and elemental valence state of the NiWN<sub>2</sub>/N-RGO film are characterized by the XPS energy spectrum, as shown in Figure 3. Figure 3A is the XPS survey of NiWN<sub>2</sub>/N-RGO. According to the binding energy from high to low, the main characteristic peaks in the XPS survey of NiWN<sub>2</sub>/N-RGO are Ni 2s, Ni 2p, O 1s, W 4p, N 1s, C 1s, W 4d and W 4f. Among these, O may come from the oxygen-containing functional groups of N-RGO. In addition to O, Ni, W, N and C are the constituent elements of NiWN<sub>2</sub>/N-RGO. There are no other elements in the XPS survey of NiWN<sub>2</sub>/N-RGO.

The Ni 2p, C 1s and N 1s spectra were analysed by the Gaussian fitting method. Figure 3B is the XPS spectrum of Ni 2p, which shows a pair of satellite peaks (denoted as sat.) and two pairs of characteristic peaks produced by spin-orbit coupling. The characteristic peaks at 873.8 and 856.5 eV correspond to Ni 2p<sub>1/2</sub> and Ni 2p<sub>3/2</sub> of Ni<sup>2+</sup>, respectively [20, 21]. The peaks at 881 and 861.7 eV are the satellite peaks of 2p<sub>1/2</sub> and Ni 2p<sub>3/2</sub> for Ni<sup>2+</sup>, respectively [20, 21]. Unexpectedly, the main peaks of Ni<sup>0</sup> at 852.7 eV are not observed. This result may mean that Ni<sup>0</sup> may not be on the surface [22] because XPS can only measure samples with a thickness of less than 5 nm on the surface.

The XPS peaks of C 1s are between 282 and 292 eV, as shown in Figure 3C. Generally, the C peaks of N-RGO can be finely split into four binding types of C. The main C 1s peak at 284.8 eV is related to graphite-like sp<sup>2</sup> C (C1) [23], indicating that most of the C atoms in N-RGO are arranged in a conjugated honeycomb lattice. The C2 (at 285.7 eV) and C3 (at 287.5 eV) peaks are assigned to N–sp<sup>2</sup> C and N–sp<sup>3</sup> C bonds, respectively [24], which indicate the formation of different C–N bond structures. The small peak at 290 eV corresponds to C–C = O [25].

As shown in Figure 4D, the N 1s peaks of the NiWN<sub>2</sub>/N-RGO samples can be fitted into four peaks centred at 396.5, 397.4, 398.2 and 400.1 eV, indicating that N atoms are in the four different bonding characters. The main peaks at 396.5 and 397.4 eV are attributed to W–N and Ni–V, respectively [26], while the peaks at 398.2 and 400.1 eV are related to pyridinic-N and pyrrolic-N, respectively. Pyridinic-N can not only provide a lone pair of electrons for the covalent  $\pi$ -bond system of N-RGO but also lower the adsorption energy of the active site for iodine atoms [27], thereby rapidly promoting the reduction of I<sub>3</sub><sup>-</sup> ions and improving the photoelectric conversion performance of DSCs.

### 3.2. Photovoltaic performance of DSCs

Sandwich-structured DSCs were obtained with a N719 dye-loaded TiO<sub>2</sub> photoanode, a NiWN<sub>2</sub>/N-RGO (or NiWN<sub>2</sub> or Pt) CE and an I<sub>3</sub><sup>-</sup>/I<sup>-</sup> electrolyte, and the photovoltaic performances of these DSCs were tested under standard conditions (AM 1.5). The results are shown in Figure 4, and the relevant parameters are listed in Table 1. Figure 4 shows that the photovoltaic performance of the DSC with NiWN<sub>2</sub> electrodes, it demonstrates a V<sub>OC</sub> of 0.76 V, a J<sub>SC</sub> of 13.36 mA·cm<sup>-2</sup>, an FF of 59.26% and an efficiency of 5.98%, which is much higher than the DSCs with WN (3.67%) [12] and nitride Ni foil (5.68%) [28]. In the case of the DSC assembled with NiWN<sub>2</sub>/N-RGO is better than that of the DSC assembled with NiWN<sub>2</sub> electrodes, with an open-circuit voltage (V<sub>OC</sub>) of 0.78 V, a short-circuit current density (J<sub>SC</sub>) of 14.47 mA·cm<sup>-2</sup>, a fill factor (FF) of 62.43% and an efficiency of 7.08%..

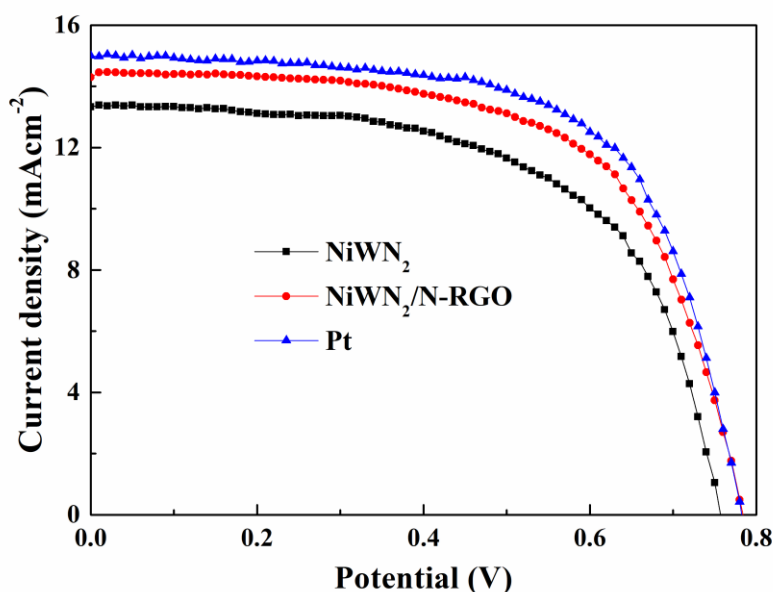


**Figure 4.** Photocurrent–voltage ( $J$ – $V$ ) curves of the DSCs with different CEs of NiWN<sub>2</sub>/N-RGO, NiWN<sub>2</sub> and Pt under 1 sun (AM 1.5) illumination.

**Table 1.** Photovoltaic parameters of the DSCs using NiWN<sub>2</sub>/N-RGO, NiWN<sub>2</sub> and Pt CEs and the simulated data from EIS.<sup>a</sup>

Samples	V <sub>oc</sub> (V)	J <sub>sc</sub> (mA/cm <sup>2</sup> )	FF (%)	Efficiency (%)	R <sub>s</sub> (Ω cm <sup>2</sup> )	R <sub>ct</sub> (Ω cm <sup>2</sup> )
NiWN <sub>2</sub>	0.76	13.36	59.26	5.98	20.7	28.1
NiWN <sub>2</sub> /N-RGO	0.78	14.47	62.43	7.08	20.3	22.7
Pt	0.78	15.04	63.68	7.48	17.9	16.7

<sup>a</sup> V<sub>oc</sub>: open-circuit voltage, J<sub>sc</sub>: short-circuit current density, FF: fill factor, efficiency: energy conversion efficiency, R<sub>s</sub>: series resistance, and R<sub>ct</sub>: charge-transfer resistance.

This enhanced performance is attributed to the synergistic effect between the NiWN<sub>2</sub> nanoparticles and N-RGO film because the N-RGO film has high conductivity and the dispersed NiWN<sub>2</sub> provides excellent catalytic ability. Under the same conditions, the DSC assembled with the Pt electrode shows an efficiency of 7.48%, with a V<sub>oc</sub> of 0.78 V, a J<sub>sc</sub> of 15.04 mA·cm<sup>-2</sup>, and an FF of 63.68%. Thus, the photoelectric properties of DSCs with NiWN<sub>2</sub>/N-RGO are comparable to those with Pt, indicating that NiWN<sub>2</sub>/N-RGO may be a favourable candidate for replacing Pt.

### 3.3. Catalytic activity of NiWN<sub>2</sub>/N-RGO

To study the relationship between the photoelectric conversion efficiency of DSCs and the NiWN<sub>2</sub>/N-RGO CE, a systematic electrochemical study of NiWN<sub>2</sub>/N-RGO was carried out by CV, EIS and Potentiodynamic polarization curves. A cyclic voltammetry (CV) test was carried out in a three-

electrode system, with Pt as the CE, Ag/Ag<sup>+</sup> as the reference electrode, and NiWN<sub>2</sub>/N-RGO (or NiWN<sub>2</sub> or Pt) as the working electrode, and the obtained CV curves are shown in Figure 5. The curves of NiWN<sub>2</sub>/N-RGO and Pt have two pairs of obvious redox peaks, which is consistent with the previous studies [12-15], indicating that NiWN<sub>2</sub>/N-RGO has good catalytic activity. In which, the negative-potential pair corresponds to the process of I<sup>-</sup>/I<sub>3</sub><sup>-</sup> (formula (1)), and the positive-potential pair corresponds to the process of I<sub>3</sub><sup>-</sup>/I<sub>2</sub> (formula (2))



We mainly focus on the peak current density and peak position difference ( $\Delta E_p$ ) between the oxidation and reduction peaks of the negative-potential pair. The larger the current density is, the higher the catalytic activity of the CE, the smaller the  $\Delta E_p$ , and the faster the reduction of I<sub>3</sub><sup>-</sup>. From Figure 5, it can be seen that the peak current density of NiWN<sub>2</sub>/N-RGO and Pt is approximately the same, which is larger than that of NiWN<sub>2</sub>, and the  $\Delta E_p$  of NiWN<sub>2</sub>/N-RGO and Pt is similar, which is smaller than that of NiWN<sub>2</sub>. These results indicate that the catalytic activity of NiWN<sub>2</sub>/N-RGO is better than that of NiWN<sub>2</sub> and similar to that of Pt.

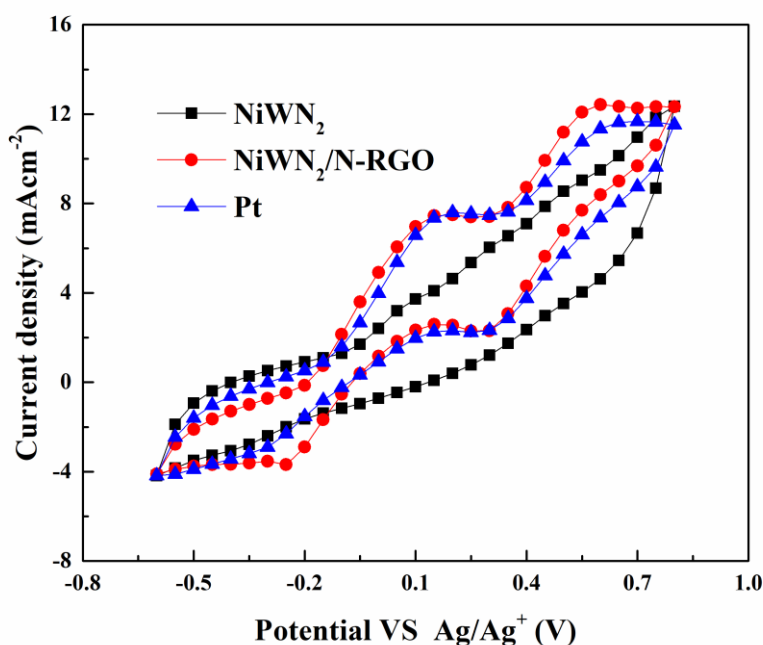


**Figure 5.** CV curves of various CEs at a scan rate of 20 mV/s in 10 mM LiI, 1 mM I<sub>2</sub>, and an acetonitrile solution containing 0.1 M LiClO<sub>4</sub> as the supporting electrolyte.

### 3.4. Electrochemical properties

The EIS test was carried out in symmetrical cells composed of two identical CEs to explore the charge transfer process of the CEs. The typical Nyquist and Bode diagrams are shown in Figures 6A, 6B and 6C. The equivalent circuits are presented in Figure 6D and 6E, and the calculated EIS parameters are listed in Table 1. In the Nyquist diagrams of Figure 6A and 6B, NiWN<sub>2</sub> and Pt show two semicircular

arcs, while NiWN<sub>2</sub>/N-RGO shows three semicircular arcs, indicating that the electrochemical transfer process of NiWN<sub>2</sub>/N-RGO may be different from that of NiWN<sub>2</sub> (or Pt); thus, their equivalent circuits may be different. The difference results from the adsorption process of iodine and triiodide on the surface of porous NiWN<sub>2</sub>/N-RGO, which is not involved in the NiWN<sub>2</sub> and Pt. This phenomenon can be seen in the previous studies [29]. The equivalent circuits of NiWN<sub>2</sub> (or Pt) and NiWN<sub>2</sub>/N-RGO are shown in Figure 6D and 6E, respectively. According to the previous work, the smaller R<sub>ct</sub>, the higher the catalytic activity of the CE, while, the smaller the Z, the faster the redox couple diffuses in the electrolyte [25, 27]. For NiWN<sub>2</sub>/N-RGO, the semicircle in the mid-frequency region represents the Nernst diffusion of the redox couple in pores, which is common in nanomaterials with porous structures [2].

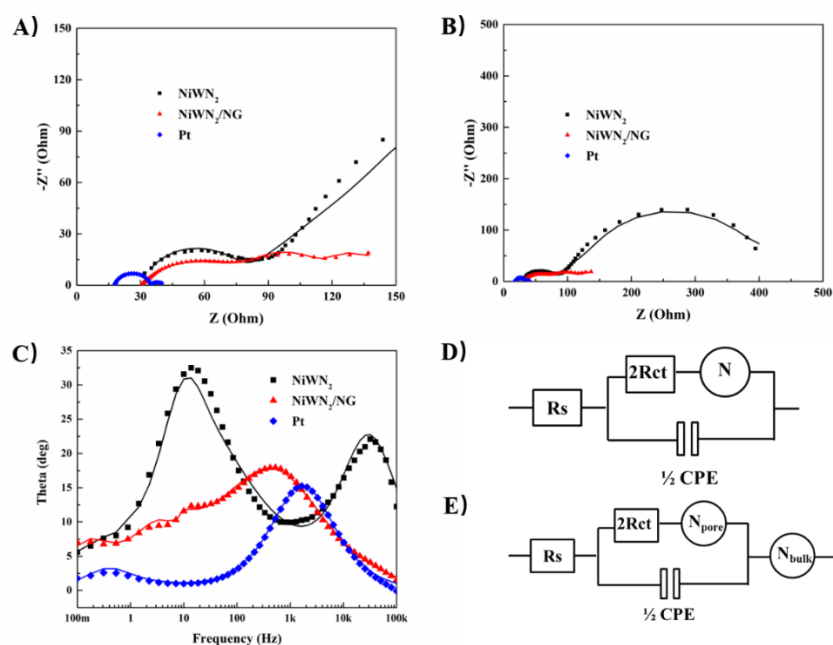


**Figure 6.** Electrochemical impedance spectroscopy (EIS) results of symmetrical cells with two identical CEs from 100 kHz to 100 mHz at V<sub>OC</sub>. The lines and symbols correspond to the simulated and experimental data, respectively. (A) Full range of the Nyquist plots. (B) Expanded range of the Nyquist plots in the high-frequency region. (C) Full range of the Bode plots. (D) Equivalent circuit for NiWN<sub>2</sub> and Pt. (E) Equivalent circuit for NiWN<sub>2</sub>/N-RGO. N<sub>bulk</sub> and N<sub>pore</sub> are the Nernst diffusion impedance values between the electrodes and within the electrode pores, respectively.

In Table 1, the R<sub>s</sub> of Pt is 17.9 Ω cm<sup>2</sup>, which is higher than that of NiWN<sub>2</sub>/N-RGO and NiWN<sub>2</sub>, indicating that the adhesion between Pt and the substrate FTO is better, and the interfacial contact resistance is low, so the FF value of DSC with Pt is the highest. Compared with NiWN<sub>2</sub>, the R<sub>s</sub> and R<sub>ct</sub> values of NiWN<sub>2</sub>/N-RGO are both smaller, indicating that the presence of N-RGO increases electron transfer and the reduction speed of I<sub>3</sub><sup>-</sup> by NiWN<sub>2</sub>; thus, electrons can be quickly transferred to the electrolyte through the CE. Similarly, the peak frequency of NiWN<sub>2</sub>/N-RGO is greater than that of

NiWN<sub>2</sub> in the high-frequency region of the Bode diagram, also indicating that NiWN<sub>2</sub>/N-RGO has better catalytic activity for catalysing I<sub>3</sub><sup>-</sup> reduction.

To further verify the electrochemical catalytic activity of the NiWN<sub>2</sub>/N-RGO electrode for the photoelectric performance of DSCs, Potentiodynamic polarization measurements were obtained in a symmetrical cell, and the resulting curves are shown in Figure 7. For a fair comparison, NiWN<sub>2</sub> and Pt were also measured under the same conditions. As shown in Figure 7, the limit diffusion current density ( $J_{lim}$ ) is the intersection of the cathodic (or anodic) branch and the Y axis, the exchange current density ( $J_0$ ) is the intersection of the tangent of the cathodic (or anodic) branch and the zero position of the abscissa. The larger the values of  $J_{lim}$  and  $J_0$  are, the better the catalytic performance of the CE [5, 12, 27]. The obtained  $J_{lim}$  and  $J_0$  of these active materials display the following order: Pt > NiWN<sub>2</sub>/N-RGO > NiWN<sub>2</sub>. According to formula (3)

$$J_0 = \frac{RT}{nFR_{ct}} \quad (3)$$

where  $R_{ct}$  is extracted from the EIS, T is the temperature, R is the gas constant, and n is the total number of individuals.

The formula above shows that  $J_0$  is inversely proportional to the electrochemical impedance  $R_{ct}$ . Thus, the tendency of  $R_{ct}$  is as follows: NiWN<sub>2</sub> > NiWN<sub>2</sub>/N-RGO > Pt, which is consistent with the EIS results.

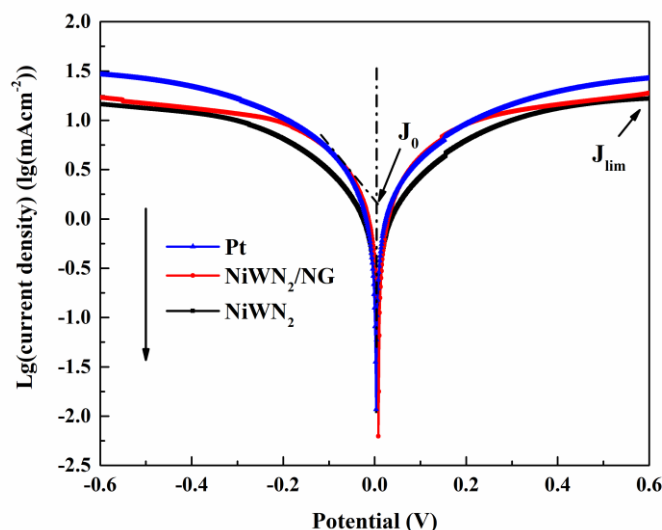


**Figure 7.** Potentiodynamic polarization curves of symmetrical cells fabricated with two identical NiWN<sub>2</sub>/N-RGO, NiWN<sub>2</sub> and Pt CEs from 0 to 0.6 V.

#### 4. CONCLUSIONS

In summary, DSCs with a NiWN<sub>2</sub>/N-RGO composite film as the CE were explored. These films were fabricated by the hydrothermal method, in which NiWN<sub>2</sub> nanoparticles were highly dispersed on the surface of N-RGO. Compared with NiWN<sub>2</sub>, the as-prepared NiWN<sub>2</sub>/N-RGO hybrid-based cell

achieved enhanced photovoltaic performance due to improved electron transport. Benefitting from the synergistic effects between the high electrocatalytic activity of NiWN<sub>2</sub> and the efficient electronic/ionic mixed conducting network provided by N-RGO, DSCs with NiWN<sub>2</sub>/N-RGO achieved an efficiency of 7.04%, which was up to 95% of that of a Pt CE (7.48%). We believe that the current work paves the way for combining nanostructured materials, which shows promise for fabricating highly efficient and low-cost CEs for DSCs.

#### ACKNOWLEDGEMENTS

This research was funded by the National Natural Science Foundation of China (grant number 51609233) and the Qingdao science and technology plan (grant number 18-2-2-9-jch).

#### References

1. L.P. Teo, M.H. Buraidah, A.K. Arof, *Ionics*, 26 (2020) 4215.
2. C.-L. Zhang, P.-X. Zhang, S.-N. Yun, Y.-L. Li, T.-S. He, *J. Inorg. Mater.*, 31 (2016) 113.
3. Y.W. Zhang, S.N. Yun, Z.Q. Wang, Y.L. Zhang, C. Wang, A. Arshad, F. Han, Y.M. Si, W. Fang, *Ceram. Int.*, 46 (2020) 15812.
4. Y.H. Yu, W.S. Wang, Y.C. Hu, X.Y. Lin, C.H. Tsai, C.J. Shih, W.C. Huang, S.M. Peng, G.H. Lee, *Dalton Trans.*, 49 (2020) 9035.
5. D.M. Tang, R.F. Zhao, J. Xie, K.H. Zhou, Y. Han, X.Y. Wu, H.Y. Wu, G.W. Diao, M. Chen, *J. Alloys Compd.*, 829 (2020) 829.
6. S.A. Salleh, M.Y.A. Rahman, Z. Yumni, T.H.T. Aziz, *Arabian J. Chem.*, 13 (2020) 5191.
7. W.W. Liu, W. Jiang, Y.C. Liu, W.J. Niu, M.C. Liu, K. Zhao, L.Y. Zhang, L. Lee, L.B. Kong, Y.L. Chueh, *ACS Appl. Energy Mater.*, 3 (2020) 3704.
8. G.R. Li, F. Wang, Q.W. Jiang, X.P. Gao, P.W. Shen, *Angew. Chem. Int. Ed.*, 49 (2010) 3653.
9. S. Prasad, G. Durai, D. Devaraj, M.S. AlSalhi, J. Theerthagiri, P. Arunachalam, M. Gurulakshmi, M. Raghavender, P. Kuppusami, *RSC Adv.*, 8 (2018) 8828.
10. H. Yan, C. Tian, L. Wang, A. Wu, M. Meng, L. Zhao, H. Fu, *Angew. Chem. Int. Ed.*, 54 (2015) 6325.
11. J. Theerthagiri, A.R. Senthil, J. Madhavan, T. Maiyalagan, *Chemelectrochem*, 2 (2015) 928.
12. G.R. Li, J. Song, G.L. Pan, X.P. Gao, *Energ Environ. Sci.*, 4 (2011) 1680.
13. X. Zheng, J. Guo, Y. Shi, F. Xiong, W.H. Zhang, T. Ma, C. Li, *Chem. Commun.*, 49 (2013) 9645.
14. Y. Wang, N. Fu, P. Ma, Y. Fang, L. Peng, X. Zhou, Y. Lin, *Appl. Surf. Sci.*, 419 (2017) 670.
15. Y. Xie, C. Zhang, G. Yang, J. Yang, X. Zhou, J. Ma, *J. Alloys Compd.*, 696 (2017) 938.
16. H. Wang, D. Wu, K. Cao, F. Wang, Z. Gao, F. Xu, K. Jiang, *Electrochim. Acta*, 251 (2017) 378.
17. V. Schwartz, S.T. Oyama, J.G.G. Chen, *J. Phys. Chem. B*, 104 (2000) 8800.
18. P., Subramanya, Herle, and, Y. N., Vasanthacharya, and, S. M., Hegde, a.J.J.o. *Alloys, Compounds*, 217 (1995) 22.
19. X.Y. Zhang, X. Chen, K.J. Zhang, S.P. Pang, X.H. Zhou, H.X. Xu, S.M. Dong, P.X. Han, Z.Y. Zhang, C.J. Zhang, G.L. Cui, *J. Mater. Chem. A*, 1 (2013) 3340.
20. N. Pauly, F. Yubero, F.J. Garcia-Garcia, S. Tougaard, *Surf. Sci.*, 644 (2016) 46.
21. Z.E. Pettifer, J.S. Quinton, W.M. Skinner, S.L. Harmer, *Appl. Surf. Sci.*, 504 (2020) 144458.
22. H.W. Nesbitt, D. Legrand, G.M. Bancroft, *Phys. Chem. Minerals* 27 (2000) 357.
23. M. Chen, L.L. Shao, Y.P. Liu, T.Z. Ren, Z.Y. Yuan, *J. Power Sources*, 283 (2015) 305.
24. R. Nonomura, T. Itoh, Y. Sato, K. Yokoyama, M. Yamamoto, T. Nishida, K. Motomiya, K. Tohji, Y. Sato, *Carbon*, 132 (2018) 539.
25. H.F. Xu, Z. Jin, *Sustain. Energy Fuels*, 4 (2020) 3604.

26. C.C. Yu, S. Ramanathan, S.T. Oyama, *J. Catal.*, 173 (1998) 1.
27. S. Hou, X. Cai, H. Wu, X. Yu, M. Peng, K. Yan, D. Zou, *Energ Environ. Sci.*, 6 (2013) 3356.
28. Q.W. Jiang, G.R. Li, S. Liu, X.P. Gao, *J. Phys. Chem. C*, 114 (2010) 13397.
29. J.D. Roy-Mayhew, D.J. Bozym, C. Punckt, I.A. Aksay, *ACS Nano*, 4 (2010) 6203.

© 2021 The Authors. Published by ESG ([www.electrochemsci.org](http://www.electrochemsci.org)). This article is an open access article distributed under the terms and conditions of the Creative Commons Attribution license (<http://creativecommons.org/licenses/by/4.0/>).